

# A rotary scanning method to evaluate grooves and porosity for nerve guide conduits based on ultrasound microscopy

Xiaoyu Yang,<sup>1</sup> Anyu Sun,<sup>1,a)</sup> Bing-feng Ju,<sup>1</sup> and Shaoning Xu<sup>2</sup>

<sup>1</sup>State Key Laboratory of Fluid Power and Mechatronic Systems, Zhejiang University, Hangzhou 310027, People's Republic of China

<sup>2</sup>Zhejiang Information Institute of Machinery Industry, Hangzhou 310027, People's Republic of China

(Received 15 September 2017; accepted 21 June 2018; published online 17 July 2018)

Grooved nerve guide conduits (NGCs) have been effective in the clinical treatment of peripheral nerve injury. They are generally fabricated from a micro-structured spinneret using a spinning process, which easily can cause a variety of pores and morphological deviation. The topography of internal grooves as well as the porosity can greatly influence the therapeutic effect. Traditional optical or scanning electron microscopy (SEM) methods can be used to image the grooves; however, these methods are destructive and require slicing NGCs to prepare specimens suitable for imaging. Moreover, lengthy experiments and large batches of NGCs are required to ensure reliable results from both *in vitro* experiments and clinical studies. In this paper, a non-destructive method for evaluating the grooves and porosity of NGCs is proposed using ultrasonic imaging combined with rotary scanning and an image analysis algorithm. Two ultrasonic methods were used: a 25-MHz point-focus ultrasonic transducer applied to observe axial cross sections of the conduits and a 100-MHz point-focus ultrasonic transducer to detect large pores caused by defects. Furthermore, a theoretical algorithm for detecting the local porosity of a conduit based on density is proposed. Herein, the proposed acoustic method and traditional optical methods are evaluated and compared. A parameter representing the specific surface area of the internal grooves is introduced and computed for both the optical and acoustic methods, and the relative errors of the computed parameter values for three different NGCs were 7.0%, 7.9%, and 15.3%. The detected location and shape of pores were consistent between the acoustic and optical methods, and greater porosity was observed in the middle of the conduit wall. In this paper, the results of the acoustic and optical methods are presented and the errors relating to the acoustic factors, device characteristics, and image processing method are further analyzed. Published by AIP Publishing.

<https://doi.org/10.1063/1.5004783>

## I. INTRODUCTION

Functional recovery following nerve injury is often hindered when a severed peripheral nerve is left untreated. Nerve guide conduits (NGCs) have been developed as a promising regenerative strategy to bridge the gap between severed nerve stumps and improve nerve regeneration following long-term peripheral nerve damage.<sup>1</sup> The nerve stumps on both sides grow inside the NGC, and their growing directions are guided by the NGC. The topographical guidance cues provided by NGCs can influence neuron development and axon outgrowth.<sup>2–6</sup> Moreover, the porous conduit wall allows the entry of nutrients into the conduit lumen, while providing a barrier between the internal regenerating tissue and tissue growing outside the conduit.<sup>2,7</sup> Porosity can be achieved using specific fabrication techniques or by selecting appropriate synthetic biodegradable polymers. The grooved texture and porosity of NGCs have been shown to significantly influence the directional outgrowth of axons.<sup>8,9</sup> A number of previously published biological and clinical studies focus on methods to evaluate grooved NGCs; however, these methods often require long cycles and large batch numbers to obtain reliable results.<sup>10,12</sup>

Current approaches to evaluate NGC grooves include optical microscopy or scanning electron microscopy (SEM).<sup>13</sup> These direct observation methods are destructive since they require NGCs to be prepared as slices to be viewed on a slide under the microscope. Intravascular ultrasound (IVUS) has also been used to image the internal surface of blood vessels by transmitting ultrasonic waves into the vessels and producing IVUS B-scans.<sup>14,15</sup> However, the ultrasonic catheter has mainly been used for arteries, which have a larger radius than NGCs. X-ray micro-tomography is another non-destructive method used to study the porosity and micromorphology of biomedical composite materials, obtaining internal images of high resolution.<sup>16</sup> While it can be used to effectively reconstruct a three-dimensional digital image of the sample in sub-micrometric resolution (up to 0.7  $\mu\text{m}$ ), it is not suitable for slender cylindrical specimens.<sup>17</sup> Moreover, the method is relatively expensive and time-consuming. Other currently applied approaches for measuring porosity include gravimetric analysis and the flux method; however, these methods are only useful for obtaining an overall porosity value. Finally, scanning acoustic microscopy (SAM) has also been widely applied to characterize various materials.<sup>18,19</sup>

In this paper, we propose an efficient nondestructive method based on SAM to evaluate the groove morphology and porosity of NGCs using ultrasound. In Sec. II A, the

<sup>a)</sup>anyusun@zju.edu.cn

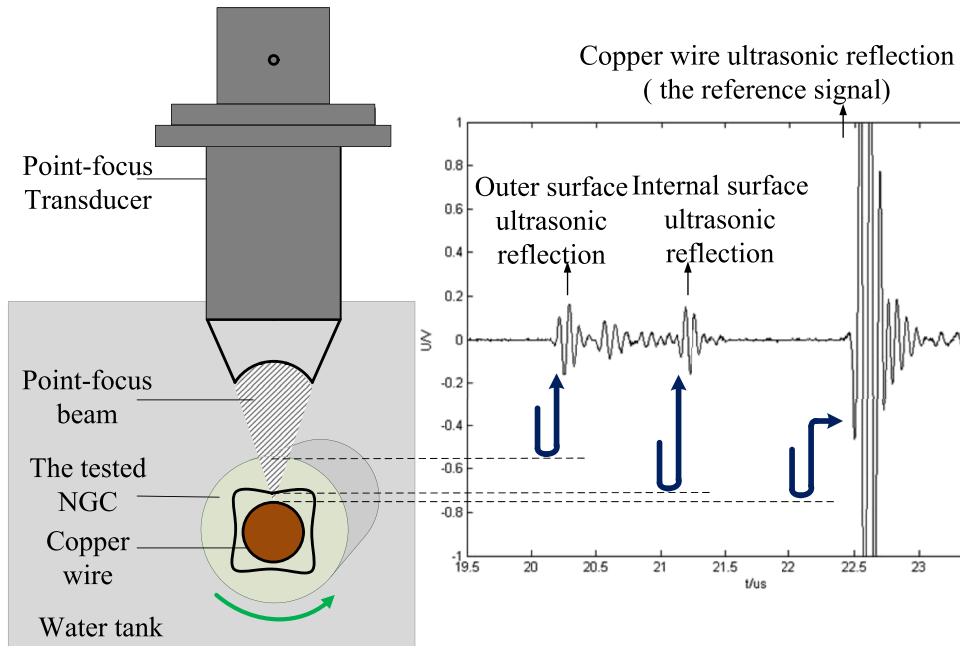


FIG. 1. Schematic of the rotary scanning method for NGCs.

rotary scanning method is introduced, which is first used to obtain raw data from axial sections of NGCs, thus avoiding strong attenuation and energy divergence associated with bias reflection. In Sec. II B, an imaging algorithm is presented to reconstruct the NGC based on the axial section images. A theoretical method to compute the local porosity is then proposed in Sec. II C. Two types of ultrasonic transducers are applied: a 25-MHz point-focus ultrasonic transducer to observe the internal micromorphology of NGCs and a 100-MHz point-focus ultrasonic transducer to detect large pores inside the NGC wall. In Sec. III, the experimental procedure is outlined, and the results are presented in Sec. IV. Finally, a discussion of the results is provided in Sec. V, and the conclusions are summarized in Sec. VI.

## II. METHODS

### A. Rotary scanning

To avoid bias reflection on the outer cylindrical convex surface, the focal wave was transmitted vertically through the outer surface of the NGC along the radial direction of the axial cross section. To identify the center of each circular axial section of the conduit, a coaxial copper wire was inserted as a reference. The centers of the wire and the NGC were on the same axis. The surface of the copper wire provides a distinct echo due to its high acoustic impedance, thus identifying the location of the wall in the reconstructed image because the distance between the surface and the center of the wire was known, which was the radius of the wire. During the scanning process, the NGC was rotated along its cylindrical axis until the entire circular section was scanned, as shown in Fig. 1.

The whole echo signal of the NGC as well as the copper wire was detected and saved as an A-scan,  $S_1(t)$ , as shown in Fig. 2(a). The wall thickness of the NGC was then computed

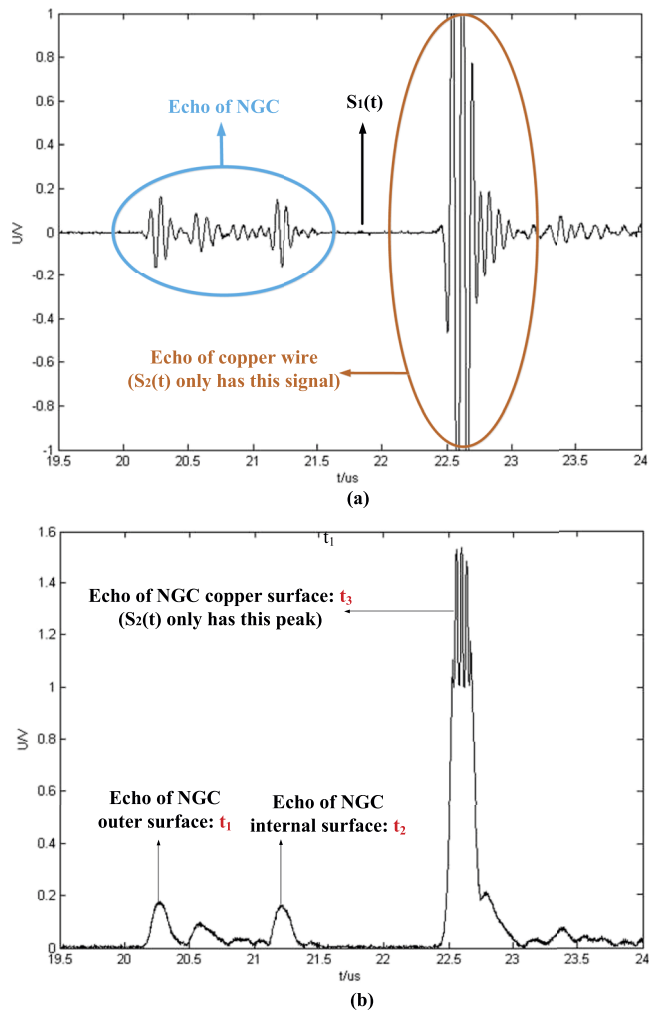


FIG. 2. (a) Whole echo signal  $S_1(t)$  of the axial cross section of an NGC with copper wire by the A-scan and (b) envelope of  $S_1(t)$ .

using the data from each A-scan. The envelope of  $S_1(t)$  can be used to locate the various peaks: The first peak at time  $t_1$  is the echo of the NGC outer surface near the transducer, the second peak at time  $t_2$  is the echo of the NGC internal surface near the transducer, and the third peak at time  $t_3$  is the echo of the copper surface.

The same method was used to detect the echo signal for the copper wire only. The envelope of  $S_2(t)$  can again be used to define the peak as  $t_4$ . The Time of Flight (TOF) in the immersion liquid of each peak is  $TOF_1 = t_1$ ,  $TOF_2 = t_3 - t_2$ , and  $TOF_3 = t_4$ . The wall thickness is

$$s = \frac{(TOF_3 - TOF_2 - TOF_1) \cdot v_0}{2}, \quad (1)$$

where  $v_0$  is the speed of sound in the liquid. The speed of sound within the scanned NGC wall is

$$v = \frac{s}{t_2 - t_1}. \quad (2)$$

Here, an approximate constant value can be used for velocity since the minor pores, which are due to the inherent porosity of the material, are evenly distributed and the main factor influencing the macro-speed of sound. Moreover, all waves

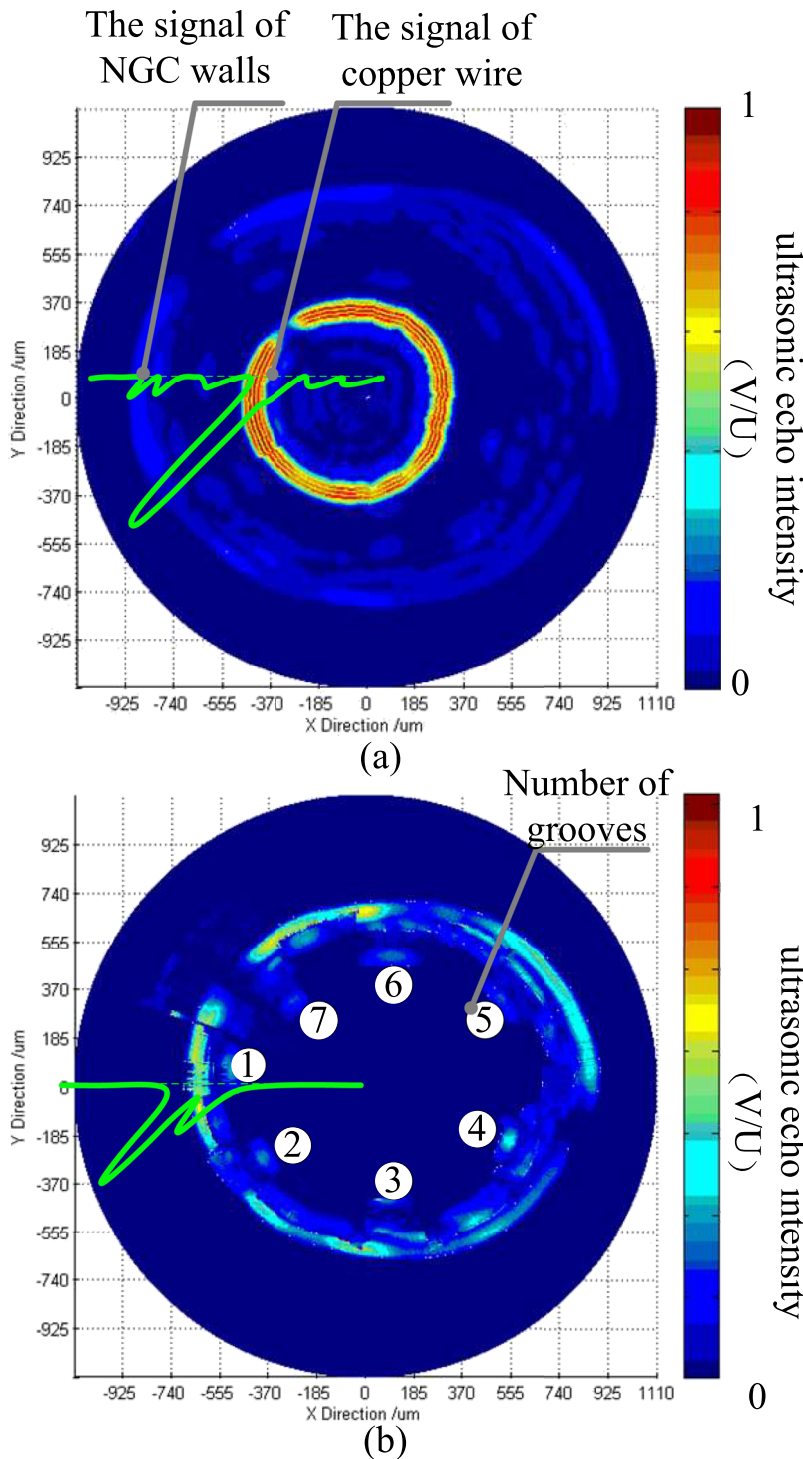


FIG. 3. (a) Map of raw A-scan data in cylindrical coordinates and (b) observation of the NGC image along the z axis using transformed A-scan data.

propagate along the radial direction of the cylinder and therefore the speed of sound is not affected by anisotropy.

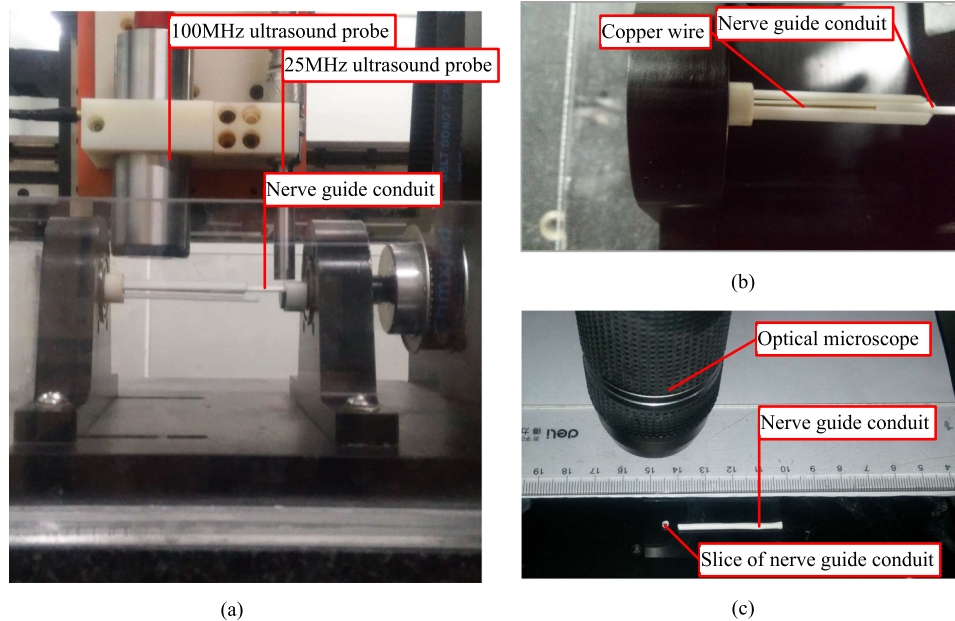
## B. Imaging algorithm

The axial cross section of the NGC is imaged using the A-scan data. Since the image scale and center of each section obtained from raw A-scan data are inaccurate, the echo signal from the copper wire is instead used as a reference to locate the center of each section. The method for obtaining the echo signal is illustrated in Fig. 2(b). For a copper wire of known diameter, the TOF of the copper wire can be transformed into the TOF within the immersion liquid at the same distance. To compensate for differences in sound velocities within the liquid and NGC, the echo of the outer surface and internal surface of the NGC can be determined according to Fig. 2(b). Thus the real distance can be transformed from the raw data using

$$\begin{bmatrix} d_1 \\ d_2 \\ d_3 \end{bmatrix} = \begin{bmatrix} 2r \\ n_2 \cdot v_0 \\ f_s \\ n_3 \cdot v \\ f_s \end{bmatrix}, \quad (3)$$

where  $d_1$  represents the radius of the copper wire,  $d_2$  represents the distance from the copper wire to the NGC wall,  $d_3$  represents the length of the NGC wall, and  $n_2$  is the raw data point between  $t_2$  and  $t_3$ . In addition,  $n_3$  is the raw data point between  $t_1$  and  $t_2$ ,  $r$  is the radius of the copper wire, and  $f_s$  is the sampling frequency. The initial point of the transformed A-scan data becomes the center of the NGC. The time scale is transformed into a more accurate distance scale. Then, the raw data can be mapped into cylindrical coordinates according to

$$\begin{bmatrix} x \\ y \end{bmatrix} = y_c \cdot \begin{bmatrix} \cos(\frac{2\pi \cdot x_c}{x_t}) \\ \sin(\frac{2\pi \cdot x_c}{x_t}) \end{bmatrix}, \quad (4)$$



where  $x$  and  $y$  are the new coordinates,  $x_c$  and  $y_c$  are the original Cartesian coordinates, and  $x_t$  is the total number of raw data points on the x axis. Thus, an image of the axial cross section of the NGC observed along the z axis can be obtained based on the colormap, as shown in Fig. 3(b).

Binarization is the operation of converting the original grayscale image into a black-and-white image and has widely been used for biological images.<sup>20</sup> The circle of the internal surface and the area surrounded by the internal surface can be computed by processing a binarized image matrix. The binarization process causes the strong and the weak echoes to look the same in the final image, as shown in Fig. 5. The ideal internal surface shape of a NGC with no grooves is round. Parameter  $k$  can be defined as

$$k = \log\left(\frac{C}{\sqrt[2]{4\pi \cdot S}}\right), \quad (5)$$

where  $C$  is the circumference of the internal surface and  $S$  is the area of the internal surface of the NGC. Parameter  $k$  of an NGC with a completely smooth internal surface should be equal to zero since the internal surface is round. Conversely, if an NGC has grooves, then  $k$  increases as the width and depth of the grooves increase. The parameter  $k$  can thus be used to evaluate the width and depth of the NGC grooves and combined with the number of grooves directly observed in the image. Therefore, the grooved NGCs can be numerically evaluated by  $k$  (Fig. 4).

## C. Porosity

While a higher frequency probe can be used to detect large pores using rotary scanning, the minor pores of the raw polymer material still cannot be detected since the ability to distinguish smaller pores is limited by the difference between attenuation and resolution.<sup>21</sup> However, another ultrasound method can be used to obtain the overall porosity derived from the density according to

FIG. 4. Physical display of the (a) ultrasound scanning device, (b) clamped NGC, and (c) slice of NGC.

$$\rho = \frac{Z}{C}, \quad (6)$$

where  $\rho$  is the local density,  $Z$  is the relative acoustic impedance with respect to some reference materials, and  $v_0$  is the speed of sound. The acoustic impedance is

$$Z = Z_w \frac{1 + R_s}{1 - R_s}, \quad (7)$$

where  $Z_w$  is the acoustic impedance of water and  $R_s$  is the reflection coefficient of the outer surface of the specimen. The reflection coefficient is<sup>22</sup>

$$R_s = \frac{V_s}{V_r} R_r, \quad (8)$$

where  $V_e$  is the amplitude of the wave reflected from the outer surface of the specimen,  $V_r$  is the amplitude of the reference wave, and  $R_r$  is the reflection coefficient of the reference, which is a constant. Whereas the current approaches measure the overall porosity, here, the porosity can be measured at different locations by altering the focus of the probe.

### III. EXPERIMENTAL PROCEDURE

In this study, a 25-MHz point-focus transducer (Olympus, Japan) with a 15 mm focal length in water and 6 mm aperture

diameter and a 100-MHz point-focus transducer (Olympus, Japan) with a 6.35 mm focal length in water and 3 mm aperture diameter were used. The resolution of the 100-MHz transducer is only high enough to image the larger pores of defects caused by the fabrication process. A sampling frequency of 4 GHz was used. Water was used as the ultrasonic couplant. The speed of sound in water is 1480.7 m/s. A stretched copper wire with a diameter of 0.6 mm was inserted into the NGC as the reference. Polyacrylonitrile (MW = 150 000 Da, Sigma) NGCs were fabricated from a micro-structured spinneret using a dry-jet wet spinning process.<sup>23</sup> The syringe is 50 mL, Model 1050 TLL SYR, provided by Hamilton Company, Switzerland. The pump is a PHD ULTRA syringe pump, provided by Harvard Apparatus, US. The grooves of the specimens had widths in the range of 100–500  $\mu\text{m}$  and depths of 10–100  $\mu\text{m}$ , as illustrated in Fig. 5. NGCs with 12, 6, or zero grooves were tested.

First, the NGC and the copper wire were concentrically installed on the rotary scanning device. The transducer was then moved until the point-focus ultrasonic beam was focused on the internal surface of the NGC. During the adjustment, the direction and focal point of the point-focus beam were observed from the real-time A-scans. Next, the closed-loop rotary scanning process was automatically started. The total 360 degrees of circular cross sectional areas were divided into 960 sets of A-scan data. The 25-MHz point-focus transducer

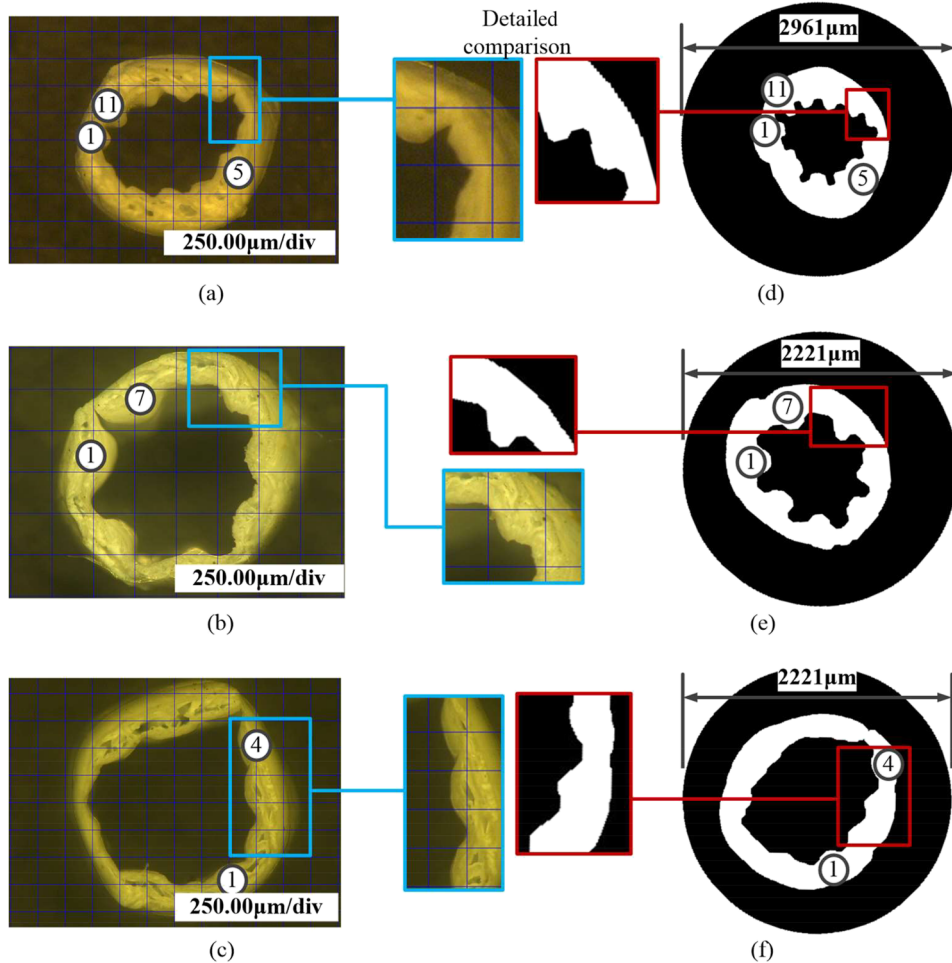


FIG. 5. Optical images of NGC slices with (a) 12 grooves, (b) 6 grooves, and (c) no grooves. The binarized ultrasonic images of the axial cross section of NGCs with (d) 12 grooves, (e) 6 grooves, and (f) no grooves using the 25-MHz transducer.

TABLE I. Image properties of the optical method.

Specimens	$N_g$	$C$ (mm)	$S$ ( $\text{mm}^2$ )	$k_O$
NGC1	4	5.00	1.500	0.061
NGC2	7	3.75	0.625	0.126
NGC3	11	4.25	0.688	0.160

was used to image the cross sections, and the 960 sets of A-scan data were processed using the image algorithm. The radius of the round image boundary can be computed as

$$r = \frac{n \cdot v_0}{f_s}, \quad (9)$$

where  $r$  is the total radius of the round image and  $n$  is the number of data points in the transformed A-scan data.

The morphology was observed under a VHX-600 digital microscope (Keyence, Japan). The 100-MHz point-focus transducer was then applied to measure the porosity. The 960 A-scan data of the NGC with no grooves were processed using the image algorithm without velocity compensation and the known center location. The overall porosity was measured.

#### IV. RESULTS

In the first experiment, three types of NGCs with 12, 6, or zero grooves were tested (Table I). The raw ultrasonic images were processed using binarization and open-close operations to obtain the final ultrasonic image, as shown in Figs. 5(d)–5(f). The internal black areas in the middle of images surrounded by the white parts (the walls of NGCs) were processed to calculate their circumference and area. Acoustic properties of the images were obtained from the internal black areas and are presented in Table II. Optical properties were obtained from the images shown in Figs. 5(a)–5(c).  $k_O$  and  $k_A$  representing the specific surface area of the internal area were then computed to measure the specific surface area of the internal grooves. The number of grooves observed using the acoustic and optical methods was almost equal. The relative errors in  $k$  were 7.0%, 7.9%, and 15.3% for 0, 6, and 12 grooves, respectively. The main cause of error was due to the changes in the relative internal surface, which increase as the number of grooves increases. In the second experiment, greater porosity was observed in the middle of the wall due to the fabrication process and is shown in both the acoustic and optical images (Fig. 6).

TABLE II. Image properties of the acoustic method.

Specimens	$N_g$	$C$ (mm)	$S$ ( $\text{mm}^2$ )	$k_A$	$\Delta k/k_A$ (%)
NGC1	4	4.943	1.495	0.057	7.0
NGC2	7	3.730	0.553	0.151	7.9
NGC3	11	4.218	0.591	0.189	15.3

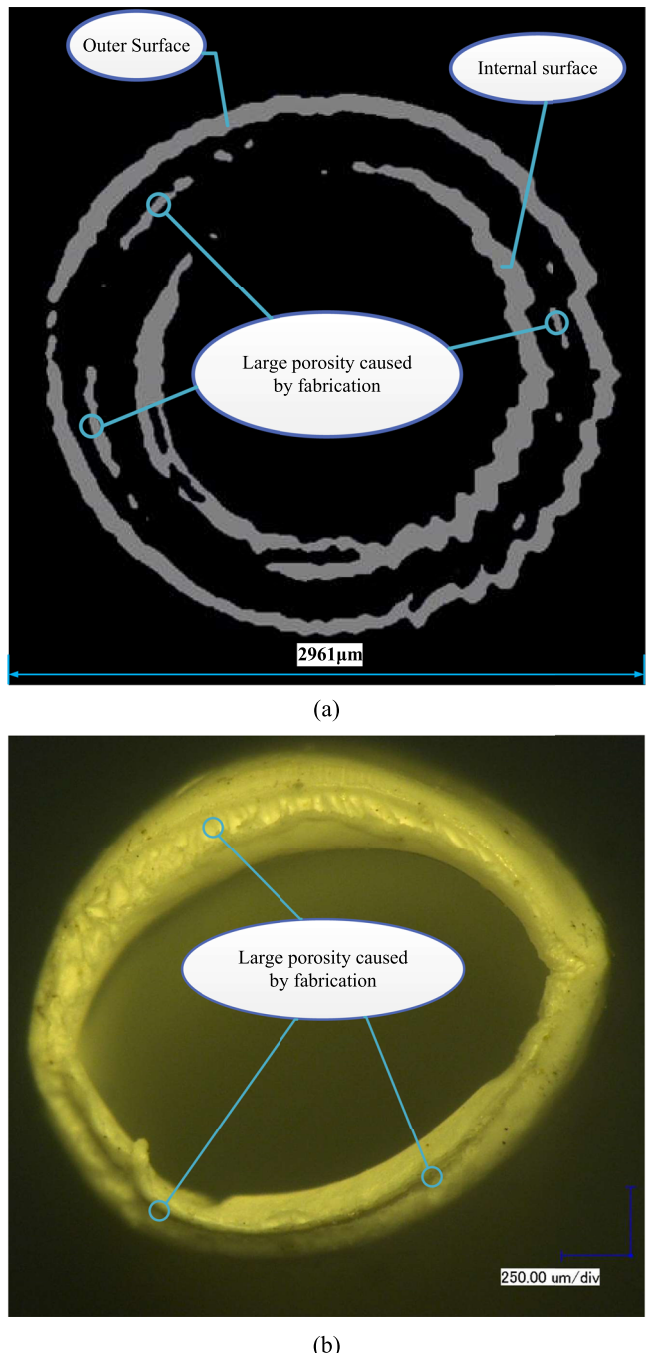


FIG. 6. (a) Binarized ultrasonic images of NGC sections with no grooves using the 100-MHz transducer and (b) the optical image of NGC slices.

#### V. DISCUSSION

The thickness of the NGC walls had an order magnitude of approximately 100  $\mu\text{m}$ . The extreme vertical resolution of the 25-MHz ultrasound can reach 30.0  $\mu\text{m}$  in water. If higher frequencies are applied, such as 50 MHz, better resolution can be achieved; however, the ultrasound may not be able to penetrate a single NGC wall due to the considerable increase in attenuation. In addition, the porous structure and liquid in the pores of the synthetic polymer enhance the energy attenuation and scattering of the ultrasonic waves.<sup>24</sup> The focal wave

propagates vertically to the outer surface rather than the internal surface, particular in areas between the peaks and troughs of the grooves, which have a weak reflection signal, as shown in Fig. 3(a). Thus a large amount of bias still occurs on the internal surface due to the acoustic waves.

When a 100-MHz ultrasound is applied, the attenuation increases and the echoes of the internal surface and copper wire become unclear. However, the 100-MHz transducer can detect the large pores created during the fabrication process owing to its higher resolution. The location and shape of the larger pores provide important feedback on the manufacturing process. So the parameters of the 25-MHz-transducer's images should be combined with the pores detected in the 100-MHz-transducer's images to give a comprehensive and rigorous evaluation. Moreover, the overall porosity derived from the density can also be measured by dividing the acoustic impedance by the acoustic velocity.

Mechanical errors and vibrations of the rotary scanning device can cause errors in the ultrasonic imaging process. Furthermore, damage to the axial cross sections of the NGCs can occur during the cutting process used to prepare the specimens for optical imaging and can thus lead to differences between the optical images and the true shape of the NGC. This type of error can be eliminated using the ultrasound method proposed in this paper. Processing raw images of NGCs without grooves is difficult since changes in the circular cross section and internal surface area are unavoidable and hard to recognize. Therefore, a new image processing method for ultrasonic images is required and should be the focus of future research.

There are some limitations to the novel method reported in this paper caused by a number of systematic errors. The measurement process also presents some limitations. First, NGCs must be relatively straight to ensure that the copper wire does not destroy the inner surface of the NGC. Second, an exceedingly large amount of data is acquired using this method leading to lengthy imaging times that are much longer than those of optical methods. Finally, the wire insertion and rotation process may cause minor scratches on the NGC wall.

With the development of biological 3D printing technologies and other fabrication methods, NGCs with more complex inner structures can be fabricated.<sup>25</sup> As such, traditional imaging methods are becoming more and more limited. The ultrasound method is useful as a viable alternative to conventional optical methods for observing the internal grooves and porosity of NGCs. However, additional research aimed at the detection of NGCs grooves is still needed to improve the current clinical applications.<sup>26,27</sup>

## VI. CONCLUSIONS

Advances in biological scaffold technology have facilitated the development of grooved NGCs, which have widely been used as a promising strategy to repair severed peripheral nerves after injury. Traditional methods to evaluate NGCs are time-consuming and destructive. In this paper, a non-destructive ultrasound imaging method based on SAM was

presented for evaluating the grooves and porosity of NGCs. The rotary scanning method addresses technical difficulties often associated with SAM including bias reflection and short transmission distances due to attenuation. An imaging algorithm was introduced to locate the center of the NGC sections and for ultrasonic velocity compensation. Ultrasonic images were obtained, and the morphologies of grooves were evaluated. Both optical and acoustic imaging methods were performed on the same NGCs and then compared. In both methods, the number of grooves was directly observed. A new parameter  $k$  was introduced to numerically describe the shape of the grooves and computed for each experiment. The groove width was negatively correlated with  $k$ , while the groove depth and the number of grooves had a positive correlation. A 100-MHz frequency ultrasound can be applied to measure porosity, and the location and shape of fabricated large pores can be directly observed. A 25-MHz frequency ultrasound can be effectively applied to observe axial sections of conduits and evaluate the grooves. Furthermore, the proposed ultrasound method can detect the overall porosity, as well as the porosity at distinct locations, based on the density of the material.

## ACKNOWLEDGMENTS

This work is supported by the National Natural Science Foundation of China (Grant Nos. 51425504, 51575488, and 51605429), Science Fund for Creative Research Groups of National Natural Science Foundation of China, No. 51521064, Zhejiang Provincial Natural Science Foundation of China, No. LZ13E050001, and Project of Application Research on Public welfare Technology, No. 2014C31086.

- <sup>1</sup>Z. Ahmed, S. Underwood, and R. A. Brown, *Tissue Eng.* **9**, 219 (2003).
- <sup>2</sup>W. A. Lackington, A. Ryan, and F. J. O'Brien, *ACS Biomater. Sci. Eng.* **3**, 1221 (2016).
- <sup>3</sup>F. Johansson, P. Carlberg, N. Danielsen, L. Montelius, and M. Kanje, *Biomaterials* **27**, 1251 (2006).
- <sup>4</sup>D. Hoffmankim, J. A. Mitchel, and R. V. Bellamkonda, *Annu. Rev. Biomed. Eng.* **12**, 203 (2010).
- <sup>5</sup>A. Kapoor, E. H. G. Caporali, P. J. A. Kenis, and M. C. Stewart, *Acta Biomater.* **6**, 2580 (2010).
- <sup>6</sup>J. Griffin, A. Carbone, R. Delgado-Rivera, S. Meiners, and K. E. Uhrich, *Acta Biomater.* **6**, 1917 (2010).
- <sup>7</sup>C. Cunha, S. Panseri, and S. Antonini, *Nanomed. Nanotechnol. Biol. Med.* **7**, 50 (2011).
- <sup>8</sup>X. Dai, L. Wang, K. Ma, B. Liu, H. Li, and K. Pan, *J. Med. Biol. Eng.* **33**, 221 (2013).
- <sup>9</sup>J. Yin, N. Coutris, and Y. Huang, *J. Neural Eng.* **9**, 056001 (2012).
- <sup>10</sup>M. Aeschlimann and L. Tettoni, *Neurocomputing* **3840**, 87 (2001).
- <sup>11</sup>G. E. Rutkowski, C. A. Miller, S. Jeftinija, and S. K. Mallapragada, *J. Neural Eng.* **1**, 151 (2004).
- <sup>12</sup>C. C. Chen, C. Y. Chan, L. S. Chen, F. J. Tsai, C. H. Yao, C. C. Tsai, and Y. S. Chen, *J. Med. Biol. Eng.* **32**, 131 (2012).
- <sup>13</sup>A. J. Neumann, T. Quinn, and S. J. Bryant, *Acta Biomater.* **39**, 1 (2016).
- <sup>14</sup>S. Sethuraman, S. R. Aglyamov, R. W. Smalling, and S. Y. Emelianov, *Ultrasound Med. Biol.* **34**, 299 (2008).
- <sup>15</sup>J. Yan, D. Lv, and Y. Cui, *J. Med. Biol. Eng.* **37**, 1 (2017).
- <sup>16</sup>S. Alonso-Sierra, R. Velzquez-Castillo, B. Milln-Malo, R. Nava, L. Bucio, A. Manzano-Ramrez, H. Cid-Luna, and E. M. Rivera-Muñoz, *Mater. Sci. Eng. C* **80**, 45 (2017).
- <sup>17</sup>E. N. Landis and D. T. Keane, *Mater. Charact.* **61**, 1305 (2010).
- <sup>18</sup>B. Bonello, G. Louis, and P. Battioni, *Rev. Sci. Instrum.* **74**, 889 (2003).
- <sup>19</sup>J. Chen, X. Bai, K. Yang, and B. F. Ju, *Rev. Sci. Instrum.* **83**, 014901 (2012).
- <sup>20</sup>S. Uchida, *Dev. Growth Differ.* **55**, 523 (2013).

- <sup>21</sup>K. P. Fuller, D. Gaspar, L. M. Delgado, A. Pandit, and D. I. Zeugolis, *Nanomedicine* **11**, 1031 (2016).
- <sup>22</sup>X. Bai, Z. Sun, A. Sun, J. Chen, and B. F. Ju, *Rev. Sci. Instrum.* **85**, 094901 (2014).
- <sup>23</sup>J. Yin, Z. Wang, W. Chai, G. Dai, H. Suo, N. Zhang, X. Wen, and Y. Huang, *J. Manuf. Sci. Eng.* **139**, 111007 (2017).
- <sup>24</sup>D. Wang, L. Wang, and P. Ding, *Ultrasonics* **70**, 266 (2016).
- <sup>25</sup>R. Mayer, P. Liacouras, A. Thomas, M. Kang, L. Lin, and C. B. S. Ii, *Rev. Sci. Instrum.* **86**, 074301 (2015).
- <sup>26</sup>M. A. Rice, K. R. Waters, and K. S. Anseth, *Acta Biomater.* **5**, 152 (2009).
- <sup>27</sup>F. G. Mitri, *Ultrasonics* **66**, 27 (2016).